

HST PHOTOMETRY OF THE GLOBULAR CLUSTER M4

RODRIGO A. IBATA^{1,2}, HARVEY B. RICHER¹, GREGORY G. FAHLMAN¹, MICHAEL BOLTE³, HOWARD E. BOND⁴, JAMES E. HESSER⁵, CARLTON PRYOR⁶, PETER B. STETSON⁵

Accepted by The Astrophysical Journal Supplement Series

ABSTRACT

This paper presents a detailed description of the acquisition and processing of a large body of imaging data for three fields in the globular cluster M4 taken with the Wide Field and Planetary Camera 2 aboard the Hubble Space Telescope. Analysis with the ALLFRAME package yielded the deepest photometry yet obtained for this cluster. The resulting data-set for 4708 stars (positions and calibrated photometry in V, I, and, in two fields, U) spanning approximately six cluster core radii is available on the AAS CD-ROM (or email a request to RAI). The scientific analysis is deferred to three companion papers, which investigate the significant white dwarf population discovered and the main sequence population.

Subject headings: globular clusters, photometry, white dwarfs, red dwarfs

1. INTRODUCTION

The refurbished Hubble Space Telescope (HST) made it possible, for the first time, to study two stellar populations that had remained almost completely unexplored from the ground even in the nearest globular clusters: the low-mass red dwarfs at the faint end of the main sequence (MS) and the white dwarfs (WDs). To understand in detail the physics of these objects, and in particular to constrain theories of the cooling of WDs and theories of the structure of faint MS stars, we undertook a study of the nearest globular cluster, M4. The scientific results of this study are presented in three companion papers: the constraints placed on the WD population are discussed in Richer *et al.* (1995) (paper 1) and Richer *et al.* (1997) (paper 2), while the investigation of the MS population is presented in Fahlman *et al.* (1998) (paper 3). The present paper details the observational data reductions performed for this study, and forms the basis from which the analysis of papers 1–3 was extracted.

2. OBSERVATIONS

The refurbished HST was used in cycle 4 (8–9 February 1995; 15–16, 29 March 1995; 4–5, 7 April 1995) to image three fields in the globular cluster M4 (HST proposal identification number 5461). The fields were chosen such that in the first field the “Planetary Camera” (PC) section of the “Wide Field and Planetary Camera” (WFPC2) mosaic was centered at the J2000 coordinates ($\alpha = 16^{\circ}23'40''$, $\delta = -26^{\circ}31'30''$), approximately at the center of M4; the second field was centered at ($\alpha = 16^{\circ}23'42''$, $\delta = -26^{\circ}30'48''$) about one core radius ($= 50''.1$ — Djorgovski 1993) from the cluster center; and the third field was centered at ($\alpha = 16^{\circ}23'56''$, $\delta = -26^{\circ}32'27''$) approximately six core radii from the center. Below, and in the accompanying papers, we refer to these fields as ‘f0’, ‘f1’ and ‘f6’, respectively. In Figure 1, the positions of these WFPC2

fields are shown superimposed on a ground-based image of M4 obtained from the Digital Sky Survey.

The cluster was observed through the filters F336W, F555W and F814W (approximately Johnson U and V and Kron-Cousins I) in fields 0 and 1; in field 6 only F555W and F814W images were obtained. The total of 28.4 hours granted for this project was divided into exposures as listed in Tables 1a, 1b and 1c. To improve the sampling of the stellar point spread functions (PSFs), all repeated exposures were “dithered”, that is, they were observed at positions slightly offset by non-integer pixel shifts from other exposures in the same field; these offsets were typically less than 10 pixels in the WF frames. No two frames were exposed with identical pointings.

3. DATA PROCESSING

Table 2 summarizes the WFPC2 detector characteristics for the observations. The images were “pipeline processed” by the Space Telescope Science Institute: the direct current bias and dark current of the charge-coupled-device (CCD) detectors were subtracted, the images were flat-fielded, and “hot-pixels” (defective regions) on the CCD were flagged as unusable. Next, the image sections heavily affected by vignetting (typically a 50 pixel wide band along the two edges of the chips that are closest to the mosaic center) were masked out. Finally all of the data frames were multiplied by a frame (obtained from the STScI) whose entries are the relative pixel areas over WFPC2; this corrects for the non-uniform area of the sky subtended by the pixels over the image plane of the camera.

The data were processed using the following photometry data reduction packages: DAOPHOT (Stetson 1987), which provided positions and initial photometry for the cluster stars; DAOMASTER (Stetson 1992) and MONTAGE2 (Stetson 1994), which were used to determine the geometrical transfor-

¹Department of Physics & Astronomy, University of British Columbia, Vancouver, B.C., V6T 1Z4. E-mail surname@astro.ubc.ca

²Present address: European Southern Observatory
Karl Schwarzschild Straße 2, D-85748 Garching bei München, Germany
Electronic mail: ribata@eso.org

³University of California, Lick Observatory, Santa Cruz, CA 9506 4. E-mail bolte@ucolick.org

⁴Space Telescope Science Institute, 3700 San Martin Drive, Baltimore, MD 21218. E-mail bond@stsci.edu

⁵National Research Council, Herzberg Institute of Astrophysics, Dominion Astrophysical Observatory, 5071 W. Saanich Road, RR5, Victoria, B.C., Canada V8X 4M6. E-mail firstname.lastname@hia.nrc.ca

⁶Rutgers, The State University of New Jersey, Department of Physics and Astronomy, PO Box 849, Piscataway, NJ 08855–0849. E-mail pryor@physics.rutgers.edu

mations between overlapping frames and to combine them to produce a clean, high signal-to-noise image; and ALLFRAME (Stetson 1994), which was used to derive the final point-spread-function (PSF) fitted photometry. In the sections below we detail these reductions.

3.1. Finding Stars

The principal objective of this experiment was to obtain the deepest possible accurate photometry of the cluster main and white dwarf sequences. The fields studied, especially those close to the cluster center, display a very non-uniform sky background. This is due in part to the crowding, but most importantly to the presence of very bright stars which produce highly-saturated images whose extended wings cover a significant fraction of the frame. Artificial star tests showed that this non-uniform sky background was the main cause of the difficulty in detecting faint local intensity peaks above the sky, thereby limiting the depth of the photometry.

Therefore, to improve the probability of finding the faint stars, all of the F555W and F814W exposures in a field were combined to form a median-filtered frame. The F336W frames were combined separately, but in a similar manner. These combined frames were obtained as follows. First, the routines FIND and PHOT within the package DAOPHOT identified and measured the positions and magnitudes of stars 10σ above the mean local sky background noise. The program DAOMASTER then yielded a six-coefficient transformation relating the position of stars on each frame to those on a chosen “master frame”; it also calculates the average magnitude offset between each frame and the master frame. Finally, the program MONTAGE2 median filtered and combined the frames using these geometrical transformations and magnitude offsets.

Figure 2a is a reproduction of the combined F555W and F814W WF3 frames in the central field (f0), while Figure 2b shows the combined F555W and F814W WF2 frames in the outermost field (f6). The difficulty of finding faint stars in the image shown in Figure 2a is evident: there are long diffraction spikes criss-crossing the image that emanate from saturated images of stars, the sky background level increases noticeably towards the center of the cluster, much of the frame is covered with charge overflow columns from highly-saturated stars, and the “wings” of the PSFs of bright stars contaminate a significant fraction of the frame.

The PSF varies considerably over the WFPC2 field; near the center of the mosaic the image profiles are round, but, towards some corners of the camera, the image profiles become significantly elongated. This means that one cannot impose stringent roundness criteria to differentiate stars from galaxies and noise peaks without losing a significant amount of valuable data. With lax roundness criteria, the standard FIND routine in DAOPHOT gave very many false detections along diffraction spikes, since the image profile of such brightness enhancements often appear stellar. However, diffraction spikes always appeared on diagonal lines on the CCDs, so the roundness parameter in FIND was altered to check for four-fold symmetry, rather than simply checking the ratio of the widths of the image along the row and column directions. (The latter is useful for eliminating charge-overflow columns and rows, but did not eliminate linear features at a 45-degree angle). No attempt was made to reject possible spurious detections that might have occurred at the intersections of Airy disks; the broad-band filters used produce low contrast rings, to which the FIND algorithm, judging from artificial star tests, was not sensitive.

After much experimentation with the roundness, sharpness and threshold parameters in the FIND routine, we concluded that we were unable to discriminate sufficiently well against false stellar detections whilst still retaining most real stars. Sufficiently far from their sources, many of the diffraction spikes fade into the sky background; however, where two such spikes cross over, the combined intensity can be raised above the detection threshold and a false detection ensues. Though the diffraction spikes are below the sky noise in the immediate neighborhood of the false detection, it can nevertheless be blatantly obvious by visual inspection of the image that the detection has occurred at the point of intersection of a pair of diffraction spikes. We decided therefore to perform a second classification by examining visually each of the candidate stars in the FIND output list (a script was used to invoke the IRAF routine IMEXAMINE). Stars were classified as either “clearly a star”, “undecided” or “certainly not a star” according to their positions with respect to diffraction spikes and according to the shapes of their profiles (the visual inspection of the profiles was especially useful where a detection occurred close to a bright star: in the strongly sloping background diffraction spikes can be difficult to trace in a grayscale image, but are easily seen in a 3-D flux map). All candidate positions deemed visually to be “certainly not a star” were removed from the lists. Note that this selection was very conservative: very few candidate stars were actually discarded (typically less than 10%), and this classification was performed *before* any photometric measurements were made.

The FIND parameters were set as follows (see Stetson 1987 and the DAOPHOT manual for a detailed explanation of the parameters): the readout noise and gain values of the detector were taken from Table 2; the low data limit was set to 10 standard deviations below the mean sky value (a larger than usual value being necessary due to the fairly variable sky background); the high data limit was set to 4090 DN; the low and high sharpness values were set to 0.2 and 1.0, respectively; and the low and high roundness values were set to -0.5 and 0.5, respectively. The improved FIND routine described above was set to find 5σ peaks above the local sky background in the combined F555W and F814W frames and in the combined F336W frames.

Finally, the star lists resulting from the combined F555W and F814W frames and from the combined F336W frames were merged to produce a “master list” for each field (the lists were summed and multiple entries — defined to be detections on the F336W frame which were less than 0.75 pixels from the position of a detection in the combined F555W and F814W frames — were removed). Some artefacts of the frames will have given rise to spurious detections that still remain in this list. Without further data, there is no sure way of removing such objects, especially towards fainter end of the data. We hope to remove most of the remaining false detections by fitting the images to a PSF. It is also very difficult to provide a quantitative estimate of the number of such spurious detections that will remain in the final photometry list. We can only remark that it seems unlikely that they would have colors that would mimic the main- and white dwarf sequences in the cluster.

Note that the median combined frames were only used to improve the finding statistics. The final photometry was not derived from these frames, but was carried out on the individual un-shifted frames as we detail in the next section.

3.2. ALLFRAME Reductions

The photometry data reduction package ALLFRAME was developed (Stetson 1994) to make optimal use of the sampling information contained in several (slightly offset) exposures of a given field. This routine fits a PSF model to all stars in all frames simultaneously, and therefore requires a knowledge of the instrumental PSF (and its variation over the frames) together with the geometrical transformations between the frames.

Since the WFPC2 instrumental PSF was believed to be relatively stable, we chose to make use of a previously constructed PSF model (Stetson, private comm.) derived from WFPC2 observations in the F336W, F555W and F814W filters of the globular cluster Omega Centauri. Bright, unsaturated stars were selected to sample the PSF, modelled as a ‘‘Moffat’’ function with a lookup table, which allows for deviations from the analytic profile. Diffraction spikes were thereby included in the PSF model, though no special effort was made to improve the signal to noise of such low contrast features. As mentioned above, the WFPC2 PSFs vary considerably with position over the mosaic and so were modeled as varying quadratically with position over each of the WFPC2 chips. The radius of the PSF function was chosen to be 14 pixels.

ALLFRAME fits the stellar profiles over a ‘‘fitting radius’’. After many experiments it was decided to use a value of 2 pixels for this parameter for both the PC and WF data. Though this compromises the photometry of bright saturated stars, in trials it produced the best photometry of the faint stars (judging by the magnitude error estimated by ALLFRAME). Other ALLFRAME parameters were set as follows: the minimum and maximum number of PSF-fitting iterations were 5 and 200, respectively; the positions of stars between frames was allowed to be refined with a 20 coefficient geometric transformation; the inner and outer radius of the sky annulus was set to 3 and 15 pixels, respectively; and the ‘‘clipping exponent’’ was set to the value 6. Two further parameters are used to help estimate the quality of the PSF fit: the ‘‘profile error’’ which was set to 6.0% (this parameter defines the contribution to the error due to PSF-mismatching), and the ‘‘percentage error’’, which was set to 0.5% (an estimate of the contribution from flat-fielding errors).

3.3. Calibrations

The ALLFRAME routine derives, among other parameters, a PSF-fitted magnitude, a magnitude uncertainty and a χ measurement for each of the frames for every star on the ‘‘master list’’.

Kelson *et al.* (1996) have shown that the detection efficiency of the WFPC2 CCDs is non-linear with exposure time. They recommend applying a correction of $(+0.05 \pm 0.007)$ magnitudes to WFPC2 images which have in excess of $160e^-$ in the mean sky. We adopt this procedure, using a linear ramp between no correction and $+0.05$ mags for those exposures where the sky counts are less than $160e^-$. The sky values (for the long exposures) in each of the frames are listed in Table 3.

The instrumental magnitudes from the different frames were combined separately for each filter as follows. First, the magnitudes and uncertainties were converted into detected counts per second. Averaging the flux measurements for a given star and weighting by the inverse-square of the uncertainties yielded the mean detected counts for that star. Then, any measurement deviating from this mean by more than four times the weighted mean error was rejected. This process was iterated until no more measurements were rejected or until a minimum number of measurements remained. This minimum number of measure-

ments was set to 4 for F336W, 8 for F555W and 4 for F814W. Finally, the weighted mean counts were converted into instrumental magnitudes.

These averaged instrumental PSF-fitted magnitudes were calibrated following the recipe of Holtzman *et al.* (1995b). First, the aperture correction was calculated for each filter and field; this correction is to account for the fact that Holtzman *et al.* (1995b) measure the flux from their standard stars with a $1''$ diameter aperture for both PC and WF data. Since the M4 star fields were rather crowded, aperture corrections could not be reliably calculated in the usual way. Instead, we constructed artificial frames using the ‘‘mknoise’’ utility in IRAF with identical sky mean and variance as the data frames (these frame statistics were measured with the SKY routine in DAOPHOT). Using the DAOPHOT routine ADDSTAR with the above-mentioned PSF as a template, 49 artificial stars were added onto the frame over a range of 5 magnitudes in intensity up to just below the saturation limit. Aperture magnitudes for these artificial stars were calculated with a $1''$ diameter aperture using the DAOPHOT routine PHOT, while PSF magnitudes were obtained using ALLFRAME with identical parameters as used for the real data. The resulting aperture corrections (in the sense $M_{PSF} - M_{APERTURE}$) are listed in Table 4; these values are added to the observed instrumental magnitudes. A check of this somewhat unconventional way of computing aperture corrections was made in field f6, where we compared the aperture-corrected PSF magnitudes with actual aperture magnitudes. All isolated stars in f6 (no neighbors within 20 pixels) with F555W and F814W PSF magnitudes brighter than 25 were chosen for this test. The aperture magnitudes of each star were combined in an identical manner to the PSF magnitudes. The F555W PSF magnitudes were found to be, on average, 0.012, 0.008, 0.005, and 0.01 magnitudes fainter than the F555W aperture magnitudes in, respectively, PC1, WF2, WF3, and WF4. An identical test for the F814W PSF magnitudes show that these are, on average, 0.007, 0.01, 0.009, and 0.002 magnitudes fainter than the F814W aperture magnitudes in, respectively, PC1, WF2, WF3, and WF4. This indicates that the aperture corrections are reliable at the ~ 0.01 magnitude level.

F336W magnitudes must be corrected for the slow degradation in UV throughput since the last decontamination date prior to observation. (Contaminants slowly accumulate on the CCD windows, reducing the transmission; this effect is reversed approximately once a month when the CCDs are deliberately heated). For an operating temperature of -88°C , Holtzman *et al.* (1995b) find that the the F336W throughput decreases by 0.0007 ± 0.0005 magnitudes per day for the PC and 0.0026 magnitudes per day for WF2 (we assume this contamination rate for all of the WF chips). The decontamination date prior to the f0 F336W observations was March 11th 1995 (24 days elapsed), so the f0 PC and WF instrumental F336W magnitudes were corrected by 0.017 and 0.062 magnitudes, respectively; while decontamination date prior to the f1 F336W observations was January 13th 1995 (26 days elapsed), so the f1 PC and WF instrumental F336W magnitudes were corrected by 0.018 and 0.068 magnitudes, respectively. Note that the uncertainty in these corrections is large, contributing to a systematic ~ 0.1 magnitude uncertainty in the F336W photometry.

A correction for the charge-transfer-efficiency (CTE) of the CCD is applied; charge is lost during the readout of the CCDs such that stars at high row numbers appear fainter than if they are observed at low row numbers. We correct for this effect by multiplying observed counts by the factor $0.02 * (y - 1) / 799.0 +$

1, where y is the row number.⁷

The standard stars used by Holtzman *et al.* (1995b) were observed with a gain level setting of 14 (see, e.g., the WFPC2 handbook). The observed counts are therefore divided by the ratio of the gain setting used by Holtzman *et al.* (1995b) to the gain setting used in the present M4 observations (these are listed in Table 2 for the four WFPC2 chips).

For comparison to photometric standards, the total extinction along the line of sight to the program stars must be known. Following the analysis in paper 2, we adopt a reddening value of $E(B-V) = 0.37$. Because this value is not negligible, the small dependence of extinction on stellar color needs to be included in the correction. Holtzman *et al.* (1995b) tabulate the extinction in the filters F336W, F555W and F814W as a function of $E(B-V)$ for an O6 spectrum and a K5 spectrum (their Tables 12A & 12B). Interpolating in these tables for $E(B-V) = 0.37$ yields: $A_{F336W} = 1.887$, $A_{F555W} = 1.143$ and $A_{F814W} = 0.659$ for an O6 star and $A_{F336W} = 1.774$, $A_{F555W} = 1.101$ and $A_{F814W} = 0.652$ for a K5 star. The instrumental magnitudes were chosen such that (in all three filters) $m = 25 - 2.5 \log(DN/s)$. In this instrumental system, we estimated that a O6 star has $F336W - F555W = 2.0$ and $F555W - F814W = 0.5$, while a K5 star has $F336W - F555W = 6.5$ and $F555W - F814W = 2.5$. A linear relation between instrumental color and extinction in the above bandpasses was thereby determined. The contribution to the total systematic uncertainty from the uncertainty in the $E(B-V)$ value is quite small; a 0.01 magnitude error in $E(B-V)$ gives rise to an error of < 0.001 magnitudes in U, V, and I.

In the case where the star has measured F336W, F555W and F814W magnitudes, the $F555W - F814W$ color is used to estimate the extinction in F555W and F814W and the $F336W - F555W$ color is used to estimate the extinction in F336W.

Finally, the synthetic transformations from instrumental extinction-corrected F555W and F814W magnitudes to Johnson V_0 and Kron-Cousins I_0 (Holtzman *et al.* 1995b, their Table 10) and observed transformations from instrumental F336W to Johnson U_0 are applied. The quoted uncertainty in the Holtzman *et al.* transformations from F555W and F814W magnitudes to V and I depends quite sensitively on color. For stars with $V - I \sim 1$, the quoted uncertainty in the transformations is relatively small, ~ 0.002 and ~ 0.004 magnitudes, in, respectively, V and I. However, for red stars with $V - I \sim 3$, this uncertainty is much larger, ~ 0.004 and ~ 0.01 magnitudes, in, respectively, V and I. The uncertainties in the transformation from F336W magnitudes to Johnson U are also color-dependent. Stars with $U - I \sim 0$, are expected to have magnitudes uncertain to ~ 0.01 . This uncertainty increases to ~ 0.08 magnitudes at $U - I \sim 5$.

The substantial overlap between fields 0 and 1 allow an internal check on the accuracy of the photometric zero-point. This is a useful exercise, as the point-spread function varies substantially over WFPC2, and in particular it allows a comparison between the PC and WF data, where the pixel scale and sky are significantly different. The difference between the 3-

sigma clipped mean magnitudes for all stars with photometric uncertainties < 0.1 mag in the two fields is: $\overline{U_{f0}} - \overline{U_{f1}} = 0.006$, $\overline{V_{f0}} - \overline{V_{f1}} = 0.012$ and $\overline{I_{f0}} - \overline{I_{f1}} = -0.009$. Note that there may be some positional mismatches, so the quoted mean differences are an upper limit to the internal systematic errors. Also, any PSF mismatch cannot give rise to a systematic error greater than these values.

To summarize, the main sources of systematic error in the V and I photometry arise from the uncertainty in the Kelson *et al.* correction for CCD non-linearity (0.007 mags), from the uncertainty in the aperture corrections (~ 0.01 mags), from the uncertainty in the CTE correction (~ 0.01 mags), from the uncertainty in the photometric transformations (~ 0.005 mags), and from any PSF mismatch ($\lesssim 0.01$ mags). A reasonable estimate of the systematic uncertainty in the V and I photometry is therefore ~ 0.04 magnitudes. The systematic uncertainty in the U-band photometry is much larger; as discussed by Holtzman *et al.* (1995a), the response from chip-to-chip and over a single chip is variable, there are variable contamination rates, and there are large uncertainties in the photometric transformations. Holtzman *et al.* estimate that UV photometry, calibrated by following their recipe, will be systematically uncertain to several tens of percent.

4. RESULTS

The complete calibrated photometry can be found on the AAS CD-ROM in the form of a 20-column ASCII table. To clarify the layout of the CD-ROM table, the printed version of this paper displays the first 10 rows of data separately in Table 5a (columns 1 to 8) and in Table 5b (columns 9 to 20). The entries in these two tables are as follows. In Table 5a, column (1) lists the sequential id number for the star, column (2) lists the field number (as defined above), column (3) gives the chip number (where a value of 1 denotes the PC chip, and values 2, 3 and 4 denote the WF1, WF2 and WF3 chips, respectively), column (4) gives the visual classification id (*cf.* Section 3.1, where the value 0 denotes that the object is “clearly a star” and the value 1 denotes “undecided”), columns (5) and (6) give the (x,y) pixel position of the object in the coordinate system of the first-observed F814W frame in that field, and columns (7) and (8) list the right ascension and declination (J2000) of the object (as determined from the STSDAS task METRIC). Table 5b lists the next 18 columns of the CD-ROM table, which give photometric quantities, in three groups of six columns. For the F336W, F555W and F814W data, respectively, columns (9), (13) & (17) list the instrumental magnitude; columns (10), (14) & (18) list the calibrated magnitude in the Johnson or Kron-Cousins system; columns (11), (15) & (19) give the rms scatter of the individual measurements that were combined to obtain the calibrated magnitude; and columns (12), (16) & (20) list the mean χ value of the PSF fit to the object. Magnitude values of 999.999 or magnitude error and χ values of 99.999 denote corrupt or unavailable data.

Figure 3 shows the calibrated color-magnitude diagram (CMD) of M4 in V vs $V - I$ (panel a) and U vs $U - I$ (panel b); only objects with magnitude uncertainties less than 0.5, χ

⁷One of us (PBS) has been involved in the calibration of WFPC2 data for the H_0 Key Project. An analysis of those data in 1996 suggested that the above procedure for CTE correction was appropriate for exposures with background levels similar to the M4 dataset. Holtzman *et al.* (1995a) find the same correction for frames with background levels of $\sim 30e^-$ to $\sim 250e^-$. After the completion of the present work, the study of Whitmore & Heyer (1997) appeared on the HST web-site; they find that charge is lost along both the row and column directions, and provide formulae for the correction of this artefact. However, we have opted not to apply this new model for CTE correction, as the purpose of the present contribution is to detail the data reduction procedure used in the companion papers 1, 2 & 3. The maximum difference between the adopted CTE correction, and that suggested by Whitmore & Heyer (1997) is ~ 0.02 magnitudes. A systematic error of ~ 0.01 magnitudes and an extra scatter of ~ 0.01 magnitudes can be expected from this mis-correction, as the M4 stars are approximately uniformly distributed over each chip.

less than 2, and that were also classified visually as stars are plotted. The cluster MS extends from the bright limit of the data at $V \sim 18$, $V-I \sim 0.9$ down to $V \sim 27$, $V-I \sim 3.0$, by which point it has almost vanished; these stars are studied in paper 3. The bulge and halo MS populations are visible as a wide band parallel to the cluster MS, but approximately 3 magnitudes fainter. The WD cooling sequence extends from $V \sim 22$, $V-I \sim 0.0$ to $V \sim 28.75$, $V-I \sim 2.0$ and is the subject of papers 1 and 2.

4.1. Photometric Accuracy

An external check of the photometric zero-point of the WFPC2 data is made by comparing the HST data to ground-based photometry (Thompson *et al.* 1990), calibrated with Landolt standards, which was acquired at the the Las Campanas Observatory (LCO) 2.5 m telescope. In Figure 4 we compare the calibrated photometry of individual stars from field 6 with the LCO data. These diagrams show quite satisfactory agreement between the two data sets. There is some evidence of a small systematic difference between the photometric zero-points of the two systems amounting to about 0.03 mags in V and 0.01 mags in I . Since it is not clear whether the ground or the space data contain this small error, we have not forced the two sets to agree, but have adopted the calibration for the *HST* data as is. The zero-point accuracy we find from these WFPC2 data is thus in fair agreement with our estimates above and with that determined from, for instance, the HST H_0 key project (Kelson *et al.* 1996).

In Figure 5 we show the magnitude uncertainties for those stars in Table 5 that have $\chi < 2$ and that were classified visually as stars. The panels show, from top to bottom, the U , V and I dependence of the magnitude uncertainties as a function of magnitude. The rise in the uncertainty at bright magnitudes occurs because the PSF is being fit to the wings of saturated stars. Towards the faint end of the diagram, the uncertainty rises due to Poisson noise in the stellar image and in the background sky. Stars whose magnitude uncertainty is much greater than the mean uncertainty at a particular magnitude are usually close to bright images or diffraction spikes. For completeness, in Figure 6 we show the PSF goodness of fit value χ derived by the ALLFRAME program (see Stetson 1994 for a precise definition of this statistic) for all of the stars in Table 5 with magnitude uncertainty $\sigma < 1.0$ mag and which were also classified visually as stars. Again, the three panels show from top to bottom the dependence of χ with magnitude for the U , V and I photometry. Note that this statistic takes on values ~ 1 for most of the stars in the data-set, implying a good fit of the PSF to the stellar image. Values of $\chi \gtrsim 2$ usually come from stars which are close to bright objects on the frame, or from galaxies.

5. INCOMPLETENESS CORRECTIONS

Since the star-finding algorithm was applied to combined F555W and F814W frames, the probability of finding faint stars will be a sensitive function of color. To probe the recovered fraction as a function of position in the CMD, artificial stars were added in the two sequences shown in the left hand panel of Figure 7, from $V = 20.41$, $V-I = 1.36$ to $V = 29.43$, $V-I = 3.55$ and from $V = 20.41$, $V-I = -0.22$ to $V = 29.43$, $V-I = 2.0$, approximating the cluster main sequence and white dwarf sequences, respectively. In each artificial star simulation, 150 MS stars and 150 WD stars were added to the WF frames and 50 MS stars and 50 WD stars were added to the PC frames. These artificial stars were added to the original data frames, *not*

the median-filtered frames. Ten such sets of simulated frames were produced for each WFPC2 field, and reduced in an identical fashion to the data frames (including visual rejection of bad detections). The right hand panel of Figure 7 shows the recovered magnitudes of the artificial stars. The scatter at a given V magnitude is greater for the artificial WDs than for the MS stars, because the latter are brighter in I . The faintest stars recovered are MS stars of $V \sim 29$. The recovered fraction of stars as a function of magnitude is given for the WD sequence in paper 2 and for the MS in paper 3.

6. CONCLUSIONS

We have presented an account of the reductions of the deepest stellar photometry yet derived for the globular cluster M4. The resulting data, tabulated in the CD-ROM accompanying this contribution, show that it is possible to obtain accurate photometry with WFPC2 to $V = 28$ in relatively crowded fields. This photometric survey is used in companion papers to study the main- and white dwarf sequences with unprecedented detail and accuracy.

APPENDIX

Due to an oversight, we did not include a table of the white dwarf luminosity function in Richer *et al.* (1997), the previous paper in this series. Table 6 is presented here to amend that oversight. The entire table is included in the AAS CD-ROM; on paper, we list only the first 10 rows. Column (1) lists the annulus number; column (2) lists the V -band magnitude; column (3) gives the completeness correction; column (4) lists the completeness-corrected cumulative luminosity function; and column (5) gives the uncertainty on the luminosity function.

This work was based on observations with the NASA/ESA *Hubble Space Telescope*, obtained at the Space Telescope Science Institute, which is operated by AURA, Inc., under NASA contract NAS5-26555. RAI expresses gratitude to the Killam Foundation (Canada) and to the Fullam (Dudley) Award for support. The research of HBR and GGF is supported in part through grants from the Natural Sciences and Engineering Research Council of Canada, while that of MB, HEB and CP is provided by NASA through the grant GO-05461.01-93A from the Space Telescope Science Institute, which is operated by the Associated Universities for Research in Astronomy, Inc., under NASA contract NAS5-26555.

REFERENCES

- Djorgovski, S., 1993 in *Structure and Dynamics of Globular Clusters*, eds. S.G. Djorgovski & G. Meylan (ASP: San Francisco), 373.
- Fahlman, G.G., Richer, H.B., Ibata, R.A., Stetson, P.B., Bell, R.A., Bolte, M., Bond, H.E., Harris, W.E., Hesser, J.E., Mandushev, G., Pryor, C. & Vandenberg, D.A., 1997, ApJ, submitted
- Holtzman, J.A., *et al.* Hester, J., Casertano, S., Trauger, J.T., Watson, A.M., Ballester, G.E., Gilda, E., Burrows, C.J., Clarke, J.T., Crisp, D., Evans, R.W., Gallagher, J.S., Griffiths, R.E., Hoessel, J.G., Matthews, L.D., Mould, J.R., Scowen, P.A., Stapelfeldt, K.R., Westphal, J.A. 1995a, PASP 107, 156
- Holtzman, J.A., Burrows, C.J., Casertano, S., Hester, J., Trauger, J.T., Watson, A.M. & Worthey, G., 1995b, PASP 107, 1065.
- Kelson, D.D., Illingworth, G.D., Freedman, W.F., Graham, J.A., Hill, R., Madore, B.F., Saha, A., Stetson, P.B., Kennicutt, R.C., Mould, J.R., Hughes, S.M., Ferrarese, L., Phelps, R., Turner, A., Cook, K.H., Ford, H., Hoessel, J.G. & Huchra, 1996, ApJ 463, 26.
- Richer, H.B., Fahlman, G.G., Ibata, R.A., Stetson, P.B., Bell, R.A., Bolte, M., Bond, H.E., Harris, W.E., Hesser, J.E., Mandushev, G., Pryor, C. & Vandenberg, D.A., 1995, ApJ 451, L17.
- Richer, H.B., Fahlman, G.G., Ibata, R.A., Pryor, C., Bell, R.A., Bolte, M., Bond, H.E., Harris, W.E., Hesser, J.E., Holland, S., Ivanans, N., Vandenberg, D.A., Wood, M., 1997, ApJ 484, 741
- Stetson, P.B., 1987, PASP 99, 613.
- Stetson, P.B., 1992, "Further Progress in CCD Photometry," in *Stellar Photometry — Current Techniques and Future Developments*, IAU Coll. 136, eds. C. J. Butler and I. Elliot, p. 291
- Stetson, P.B., 1994, PASP 106, 250.
- Thompson *et al.* 1990, unpublished photometry.

TABLE 1A
EXPOSURE TIMES, FIELD F0

| RA (J2000) | DEC (J2000) | Filter | Exposure time (sec) | Observation start time | STScI exposure code |
|-----------------|----------------|--------|------------------------|---------------------------|------------------------|
| 16 23 40.05 | -26 31 30.29 | F814W | 600 | 04 Apr 1995 9:29AM | U2HE0101T |
| 16 23 40.05 | -26 31 30.29 | F336W | 1300 | 04 Apr 1995 9:43AM | U2HE0102T |
| 16 23 40.05 | -26 31 30.25 | F814W | 700 | 04 Apr 1995 10:52AM | U2HE0103T |
| 16 23 40.05 | -26 31 30.25 | F336W | 1500 | 04 Apr 1995 11:07AM | U2HE0104T |
| 16 23 40.06 | -26 31 30.26 | F814W | 700 | 04 Apr 1995 12:28PM | U2HE0105T |
| 16 23 40.06 | -26 31 30.26 | F336W | 1500 | 04 Apr 1995 12:43PM | U2HE0106T |
| 16 23 40.06 | -26 31 30.32 | F814W | 700 | 04 Apr 1995 2:05PM | U2HE0107T |
| 16 23 40.06 | -26 31 30.32 | F336W | 1500 | 04 Apr 1995 2:20PM | U2HE0108T |
| 16 23 40.06 | -26 31 30.42 | F814W | 700 | 04 Apr 1995 3:41PM | U2HE0109T |
| 16 23 40.06 | -26 31 30.42 | F336W | 1500 | 04 Apr 1995 3:56PM | U2HE010AM |
| 16 23 40.06 | -26 31 30.46 | F814W | 700 | 04 Apr 1995 5:18PM | U2HE010BM |
| 16 23 40.06 | -26 31 30.46 | F336W | 1500 | 04 Apr 1995 5:33PM | U2HE010CM |
| 16 23 40.05 | -26 31 30.44 | F814W | 700 | 04 Apr 1995 6:55PM | U2HE010DN |
| 16 23 40.05 | -26 31 30.44 | F336W | 1500 | 04 Apr 1995 7:10PM | U2HE010EN |
| 16 23 40.05 | -26 31 30.38 | F814W | 700 | 04 Apr 1995 8:32PM | U2HE010FP |
| 16 23 40.05 | -26 31 30.38 | F336W | 1500 | 04 Apr 1995 8:47PM | U2HE010GP |
| 16 23 40.05 | -26 31 30.29 | F555W | 1000 | 05 Apr 1995 9:35AM | U2HE0201T |
| 16 23 40.05 | -26 31 30.26 | F555W | 1000 | 05 Apr 1995 9:57AM | U2HE0202T |
| 16 23 40.06 | -26 31 30.27 | F555W | 1000 | 05 Apr 1995 11:00AM | U2HE0203T |
| 16 23 40.06 | -26 31 30.28 | F555W | 1000 | 05 Apr 1995 11:22AM | U2HE0204T |
| 16 23 40.07 | -26 31 30.29 | F555W | 1000 | 05 Apr 1995 12:37PM | U2HE0205T |
| 16 23 40.07 | -26 31 30.33 | F555W | 1000 | 05 Apr 1995 12:59PM | U2HE0206T |
| 16 23 40.07 | -26 31 30.39 | F555W | 1000 | 05 Apr 1995 2:14PM | U2HE0207T |
| 16 23 40.07 | -26 31 30.46 | F555W | 1000 | 05 Apr 1995 2:36PM | U2HE0208T |
| 16 23 40.07 | -26 31 30.52 | F555W | 1000 | 05 Apr 1995 3:50PM | U2HE0209T |
| 16 23 40.06 | -26 31 30.55 | F555W | 1000 | 05 Apr 1995 4:12PM | U2HE020AT |
| 16 23 40.06 | -26 31 30.54 | F555W | 1000 | 05 Apr 1995 5:27PM | U2HE020BT |
| 16 23 40.05 | -26 31 30.52 | F555W | 1000 | 05 Apr 1995 5:49PM | U2HE020CT |
| 16 23 40.05 | -26 31 30.52 | F555W | 1000 | 05 Apr 1995 7:03PM | U2HE020DN |
| 16 23 40.05 | -26 31 30.48 | F555W | 1000 | 05 Apr 1995 7:25PM | U2HE020EN |
| 16 23 40.05 | -26 31 30.41 | F555W | 1000 | 05 Apr 1995 8:40PM | U2HE020FN |
| Total exposure: | | F336W | 11800 | | |
| | | F555W | 15000 | | |
| | | F814W | 5500 | | |

TABLE 1B
EXPOSURE TIMES, FIELD F1

| RA (J2000) | DEC (J2000) | Filter | Exposure time (sec) | Observation start time | STScI exposure code |
|-----------------|----------------|--------|------------------------|---------------------------|------------------------|
| 16 23 42.84 | -26 30 48.93 | F814W | 600 | 08 Feb 1995 4:48PM | U2HE0301T |
| 16 23 42.84 | -26 30 48.93 | F336W | 1300 | 08 Feb 1995 5:02PM | U2HE0302T |
| 16 23 42.84 | -26 30 48.89 | F814W | 700 | 08 Feb 1995 6:15PM | U2HE0303T |
| 16 23 42.84 | -26 30 48.89 | F336W | 1500 | 08 Feb 1995 6:30PM | U2HE0304T |
| 16 23 42.85 | -26 30 48.91 | F814W | 700 | 08 Feb 1995 7:52PM | U2HE0305T |
| 16 23 42.85 | -26 30 48.91 | F336W | 1500 | 08 Feb 1995 8:07PM | U2HE0306T |
| 16 23 42.85 | -26 30 48.97 | F814W | 700 | 08 Feb 1995 9:28PM | U2HE0307T |
| 16 23 42.85 | -26 30 48.97 | F336W | 1500 | 08 Feb 1995 9:43PM | U2HE0308T |
| 16 23 42.85 | -26 30 49.06 | F814W | 700 | 08 Feb 1995 11:05PM | U2HE0309T |
| 16 23 42.85 | -26 30 49.06 | F336W | 1500 | 08 Feb 1995 11:20PM | U2HE030AT |
| 16 23 42.84 | -26 30 49.10 | F814W | 700 | 09 Feb 1995 12:41AM | U2HE030BT |
| 16 23 42.84 | -26 30 49.10 | F336W | 1500 | 09 Feb 1995 12:56AM | U2HE030CT |
| 16 23 42.84 | -26 30 49.09 | F814W | 700 | 09 Feb 1995 2:20AM | U2HE030DT |
| 16 23 42.84 | -26 30 49.09 | F336W | 1500 | 09 Feb 1995 2:35AM | U2HE030ET |
| 16 23 42.83 | -26 30 49.03 | F814W | 700 | 09 Feb 1995 3:56AM | U2HE030FT |
| 16 23 42.83 | -26 30 49.03 | F336W | 1500 | 09 Feb 1995 4:11AM | U2HE030GT |
| 16 23 42.83 | -26 30 48.99 | F555W | 1000 | 07 Apr 1995 8:38AM | U2HE0401T |
| 16 23 42.83 | -26 30 48.96 | F555W | 1000 | 07 Apr 1995 9:41AM | U2HE0402T |
| 16 23 42.84 | -26 30 48.97 | F555W | 1000 | 07 Apr 1995 10:03AM | U2HE0403T |
| 16 23 42.84 | -26 30 48.98 | F555W | 1000 | 07 Apr 1995 11:18AM | U2HE0404T |
| 16 23 42.85 | -26 30 48.99 | F555W | 1000 | 07 Apr 1995 11:40AM | U2HE0405T |
| 16 23 42.85 | -26 30 49.03 | F555W | 1000 | 07 Apr 1995 12:55PM | U2HE0406T |
| 16 23 42.85 | -26 30 49.09 | F555W | 1000 | 07 Apr 1995 1:17PM | U2HE0407T |
| 16 23 42.85 | -26 30 49.16 | F555W | 1000 | 07 Apr 1995 2:31PM | U2HE0408T |
| 16 23 42.85 | -26 30 49.22 | F555W | 1000 | 07 Apr 1995 2:53PM | U2HE0409T |
| 16 23 42.84 | -26 30 49.25 | F555W | 1000 | 07 Apr 1995 4:08PM | U2HE040AT |
| 16 23 42.84 | -26 30 49.24 | F555W | 1000 | 07 Apr 1995 4:30PM | U2HE040BT |
| 16 23 42.83 | -26 30 49.22 | F555W | 1000 | 07 Apr 1995 5:44PM | U2HE040CT |
| 16 23 42.83 | -26 30 49.22 | F555W | 1000 | 07 Apr 1995 6:06PM | U2HE040DT |
| 16 23 42.83 | -26 30 49.18 | F555W | 1000 | 07 Apr 1995 7:21PM | U2HE040ET |
| 16 23 42.83 | -26 30 49.11 | F555W | 1000 | 07 Apr 1995 7:43PM | U2HE040FT |
| Total exposure: | | F336W | 11800 | | |
| | | F555W | 15000 | | |
| | | F814W | 5500 | | |

TABLE 1C
EXPOSURE TIMES, FIELD F6

| RA (J2000) | DEC (J2000) | Filter | Exposure time (sec) | Observation start time | STScI exposure code |
|-----------------|----------------|--------|------------------------|---------------------------|------------------------|
| 16 23 56.89 | -26 32 27.89 | F555W | 2100 | 04 Apr 1995 10:22PM | U2HE0501T |
| 16 23 56.89 | -26 32 27.86 | F555W | 2100 | 04 Apr 1995 11:49PM | U2HE0502T |
| 16 23 56.90 | -26 32 27.87 | F555W | 2100 | 05 Apr 1995 1:24AM | U2HE0503T |
| 16 23 56.90 | -26 32 27.88 | F555W | 2100 | 05 Apr 1995 2:58AM | U2HE0504T |
| 16 23 56.91 | -26 32 27.89 | F555W | 2100 | 05 Apr 1995 4:34AM | U2HE0505T |
| 16 23 56.91 | -26 32 27.93 | F555W | 2100 | 05 Apr 1995 6:11AM | U2HE0506T |
| 16 23 56.91 | -26 32 27.99 | F555W | 2100 | 05 Apr 1995 7:47AM | U2HE0507T |
| 16 23 56.91 | -26 32 28.06 | F555W | 2100 | 29 Mar 1995 5:26AM | U2HE0601T |
| 16 23 56.91 | -26 32 28.12 | F555W | 2100 | 29 Mar 1995 6:52AM | U2HE0602T |
| 16 23 56.90 | -26 32 28.15 | F555W | 2100 | 29 Mar 1995 8:28AM | U2HE0603T |
| 16 23 56.90 | -26 32 28.14 | F555W | 2100 | 29 Mar 1995 10:05AM | U2HE0604T |
| 16 23 56.90 | -26 32 28.12 | F555W | 2100 | 29 Mar 1995 11:41AM | U2HE0605T |
| 16 23 56.89 | -26 32 28.12 | F555W | 2100 | 29 Mar 1995 1:18PM | U2HE0606T |
| 16 23 56.89 | -26 32 28.08 | F555W | 2100 | 29 Mar 1995 2:54PM | U2HE0607T |
| 16 23 56.89 | -26 32 28.01 | F555W | 2100 | 29 Mar 1995 4:31PM | U2HE0608T |
| 16 23 56.90 | -26 32 27.83 | F814W | 800 | 15 Mar 1995 6:11PM | U2HE0701T |
| 16 23 56.90 | -26 32 27.79 | F814W | 800 | 15 Mar 1995 6:30PM | U2HE0702T |
| 16 23 56.91 | -26 32 27.81 | F814W | 800 | 15 Mar 1995 7:36PM | U2HE0703T |
| 16 23 56.91 | -26 32 27.87 | F814W | 800 | 15 Mar 1995 7:55PM | U2HE0704T |
| 16 23 56.91 | -26 32 27.96 | F814W | 800 | 15 Mar 1995 9:18PM | U2HE0705T |
| 16 23 56.91 | -26 32 28.00 | F814W | 800 | 15 Mar 1995 9:37PM | U2HE0706T |
| 16 23 56.90 | -26 32 27.99 | F814W | 800 | 15 Mar 1995 11:01PM | U2HE0707T |
| 16 23 56.90 | -26 32 27.93 | F814W | 800 | 15 Mar 1995 11:20PM | U2HE0708T |
| 16 23 56.90 | -26 32 27.90 | F814W | 800 | 16 Mar 1995 12:43AM | U2HE0709T |
| Total exposure: | | | | | |
| | | F555W | 31500 | | |
| | | F814W | 7200 | | |

TABLE 2
WFPC2 DETECTOR CHARACTERISTICS

| Chip | pixel size (") | field size (") | gain (e^- /ADU) | read noise ADU |
|------|-------------------|-------------------|-----------------------|-------------------|
| PC1 | 0.046 | 37 × 37 | 7.12 | 0.74 |
| WF2 | 0.1 | 80 × 80 | 7.12 | 0.77 |
| WF3 | 0.1 | 80 × 80 | 6.90 | 0.76 |
| WF4 | 0.1 | 80 × 80 | 7.10 | 0.73 |

TABLE 3
MEAN SKY IN FRAMES

| Chip | f0 | | | f1 | | | f6 | |
|------|-------|-------|-------|-------|-------|-------|-------|-------|
| | F336W | F555W | F814W | F336W | F555W | F814W | F555W | F814W |
| PC1 | 6. | 56. | 49. | 4. | 48. | 48. | 60. | 26. |
| WF2 | 14. | 154. | 118. | 16. | 165. | 175. | 296. | 119. |
| WF3 | 16. | 160. | 119. | 15. | 148. | 154. | 286. | 116. |
| WF4 | 16. | 174. | 143. | 19. | 181. | 190. | 290. | 119. |

TABLE 4
APERTURE CORRECTIONS

| Chip | f0 | | | f1 | | | f6 | |
|------|-------|-------|-------|-------|-------|-------|-------|-------|
| | F336W | F555W | F814W | F336W | F555W | F814W | F555W | F814W |
| PC1 | 0.030 | 0.024 | 0.023 | 0.029 | 0.027 | 0.021 | 0.029 | 0.018 |
| WF2 | 0.057 | 0.047 | 0.047 | 0.060 | 0.040 | 0.046 | 0.037 | 0.050 |
| WF3 | 0.069 | 0.044 | 0.055 | 0.060 | 0.039 | 0.046 | 0.042 | 0.051 |
| WF4 | 0.056 | 0.053 | 0.051 | 0.053 | 0.046 | 0.048 | 0.053 | 0.055 |

TABLE 5A
THE PHOTOMETRY

| id (1) | field (2) | chip (3) | class (4) | x (5) | y (6) | RA (2000) (7) | DEC (2000) (8) |
|-----------|--------------|-------------|--------------|----------|----------|------------------|-------------------|
| 1 | 0 | 1 | 0 | 620.99 | 65.79 | 245.90794 | -26.52923 |
| 2 | 0 | 1 | 0 | 639.38 | 82.59 | 245.90759 | -26.52919 |
| 3 | 0 | 1 | 0 | 457.95 | 66.56 | 245.90981 | -26.52804 |
| 4 | 0 | 1 | 0 | 83.86 | 69.46 | 245.91406 | -26.52529 |
| 5 | 0 | 1 | 0 | 85.77 | 75.06 | 245.91400 | -26.52524 |
| 6 | 0 | 1 | 0 | 339.62 | 76.05 | 245.91109 | -26.52708 |
| 7 | 0 | 1 | 0 | 761.35 | 81.85 | 245.90620 | -26.53007 |
| 8 | 0 | 1 | 0 | 357.29 | 83.16 | 245.91083 | -26.52714 |
| 9 | 0 | 1 | 0 | 523.63 | 83.70 | 245.90892 | -26.52834 |
| 10 | 0 | 1 | 0 | 99.49 | 95.67 | 245.91368 | -26.52513 |

TABLE 5B
THE PHOTOMETRY (FURTHER COLUMNS)

| F336W (9) | U (10) | σ_U (11) | χ_U (12) | F555W (13) | V (14) | σ_V (15) | χ_V (16) | F814W (17) | I (18) | σ_I (19) | χ_I (20) |
|--------------|-----------|--------------------|------------------|---------------|-----------|--------------------|------------------|---------------|-----------|--------------------|------------------|
| 21.216 | 21.130 | 99.999 | 6.320 | 19.794 | 19.788 | 0.050 | 1.516 | 18.566 | 18.531 | 0.090 | 1.256 |
| 25.573 | 27.057 | 2.062 | 1.244 | 18.006 | 17.994 | 0.105 | 1.026 | 16.456 | 16.413 | 0.154 | 1.570 |
| 24.889 | 25.119 | 1.336 | 1.502 | 19.284 | 19.277 | 0.027 | 1.164 | 17.995 | 17.959 | 0.021 | 1.256 |
| 24.579 | 25.002 | 0.582 | 2.941 | 18.506 | 18.506 | 0.008 | 1.586 | 17.549 | 17.519 | 0.000 | 1.080 |
| 24.788 | 25.246 | 1.362 | 1.893 | 18.641 | 18.637 | 0.024 | 1.266 | 17.498 | 17.465 | 0.028 | 0.968 |
| 25.836 | 26.309 | 0.712 | 1.235 | 19.659 | 19.650 | 0.035 | 1.234 | 18.269 | 18.232 | 0.023 | 0.861 |
| 26.035 | 26.364 | 1.306 | 1.214 | 20.176 | 20.164 | 0.034 | 1.402 | 18.641 | 18.600 | 0.017 | 0.952 |
| 25.734 | 26.262 | 0.717 | 0.942 | 19.449 | 19.440 | 0.048 | 1.026 | 18.095 | 18.059 | 0.015 | 0.792 |
| 23.356 | 23.426 | 0.356 | 1.865 | 18.258 | 18.258 | 0.098 | 1.029 | 17.303 | 17.274 | 0.270 | 1.086 |
| 25.894 | 27.140 | 1.572 | 1.197 | 18.574 | 18.568 | 0.043 | 1.194 | 17.372 | 17.338 | 0.017 | 0.914 |

TABLE 6
CUMULATIVE WHITE DWARF LUMINOSITY FUNCTION

| Annulus | V | completeness | Φ | $\sigma(\Phi)$ |
|---------|----------|--------------|--------|----------------|
| 1 | 22.64200 | 0.47807 | 2.092 | 0.363 |
| 1 | 22.89200 | 0.50610 | 4.068 | 0.497 |
| 1 | 22.89900 | 0.50639 | 6.042 | 0.601 |
| 1 | 23.11800 | 0.50451 | 8.025 | 0.690 |
| 1 | 23.30400 | 0.48907 | 10.069 | 0.774 |
| 1 | 23.37500 | 0.48058 | 12.150 | 0.853 |
| 1 | 23.67400 | 0.43368 | 14.456 | 0.942 |
| 1 | 23.67900 | 0.43278 | 16.767 | 1.024 |
| 1 | 23.77200 | 0.41556 | 19.173 | 1.107 |
| 1 | 23.88900 | 0.39290 | 21.718 | 1.195 |

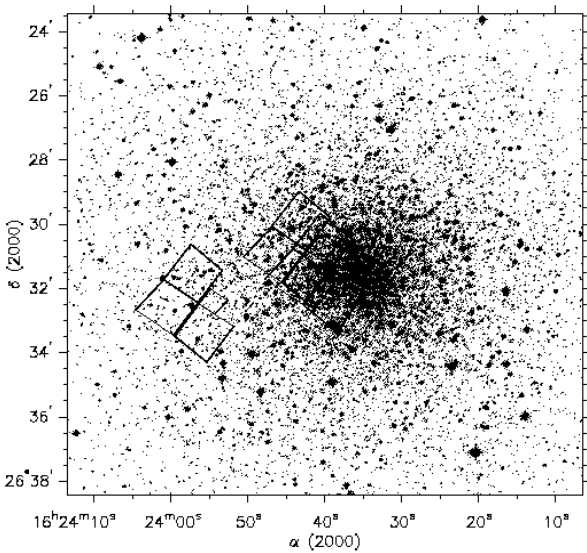


FIG. 1.— The WFPC2 field positions are shown superimposed on a ground-based image of M4 extracted from the Digital Sky Survey (second generation). The positions of the vertices of the WFPC2 fields were derived using the STSDAS task “METRIC”. The non-rectangular projection of the CCDs on the sky is due to the optical distortion of the WFPC2 camera.

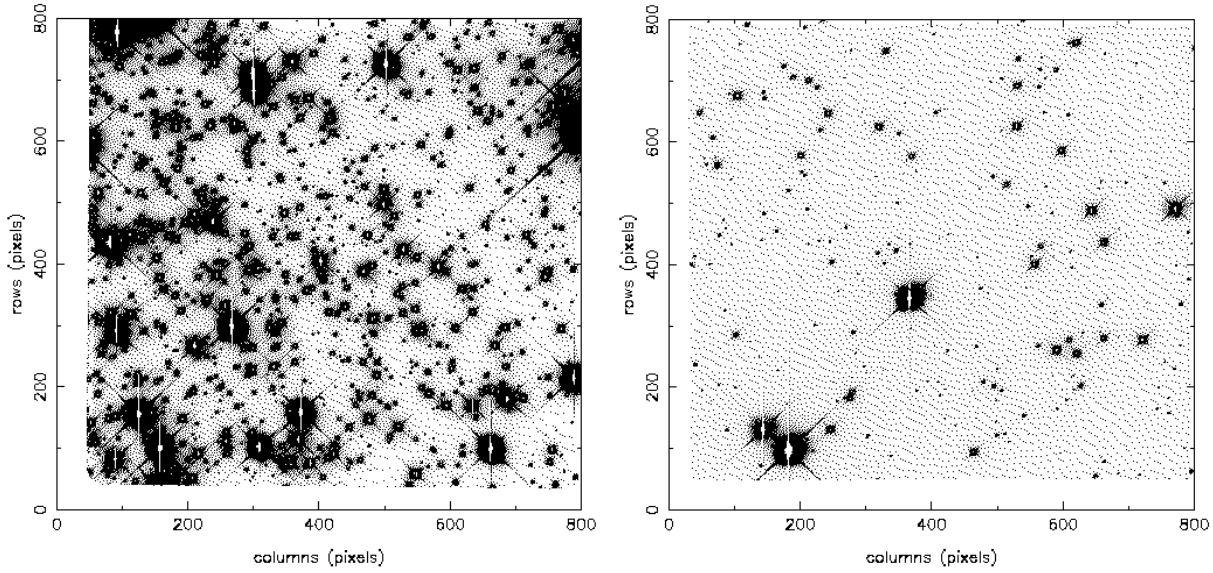


FIG. 2.— Panel (a) shows a median-filtered image combined from all of the available F555W and F814W exposures in the WF3 chip in field f0. Obtaining good photometry in such situations is clearly difficult, as the field is crowded, there are many long diffraction spikes, the sky background is not uniform, and the diffuse halos that surround many bright stars contaminate a large fraction of the image. For comparison, in panel (b) we display the combined F555W and F814W data from the WF2 chip in field f6, which yielded the deepest photometry. The white patches on these representations correspond to regions where the CCD was saturated.

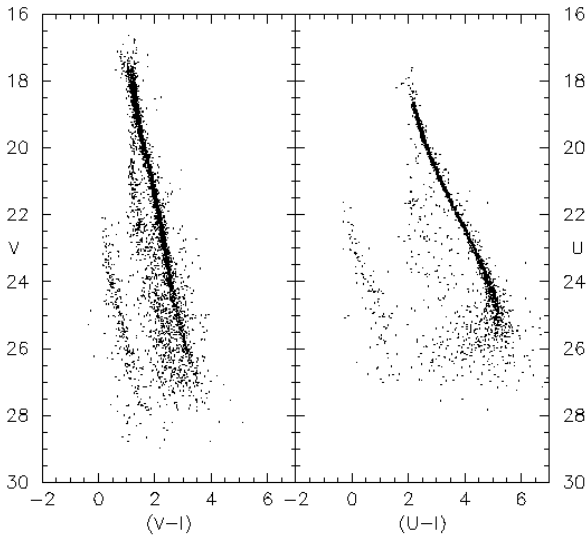


FIG. 3.— The calibrated photometry is displayed. The left-hand panel shows the V vs $V-I$ CMD containing data from all of the observed fields, while the right hand panel gives the U vs $U-I$ CMD for fields f0 and f1. All objects plotted on these diagrams have photometric uncertainties of less than 0.5 mags, $\chi < 2.0$, and were confirmed visually to be stars.

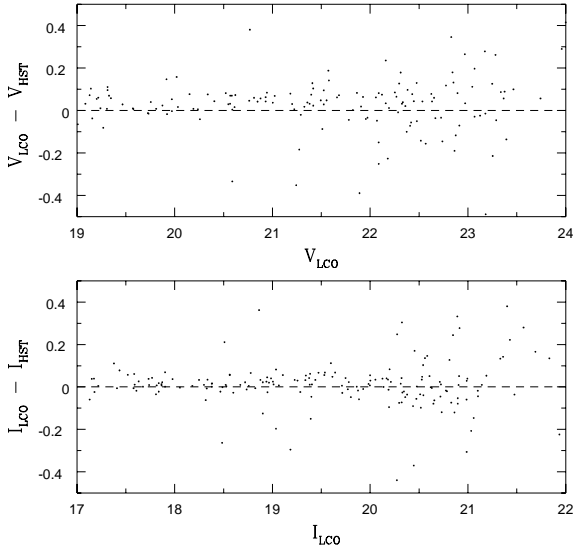


FIG. 4.— A comparison between ground-based V and I photometry from the Las Campanas 2.5 meter telescope and that from *HST*. All of the stars shown are from field 6.

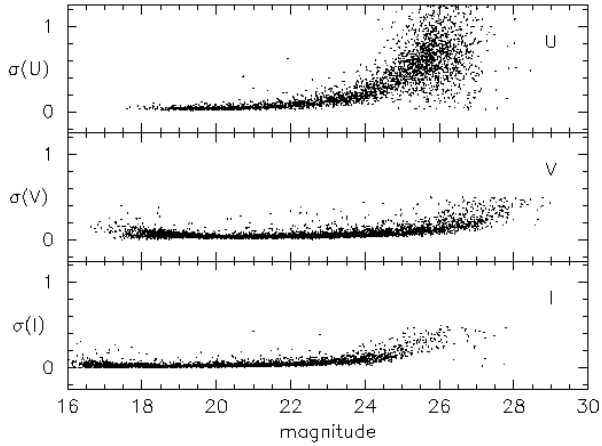


FIG. 5.— The panels show, from top to bottom, the dependence on magnitude for the U, V, and I photometry of the magnitude uncertainties for all stars in Table 5 that have $\chi < 2$ and that were classified visually as stars.

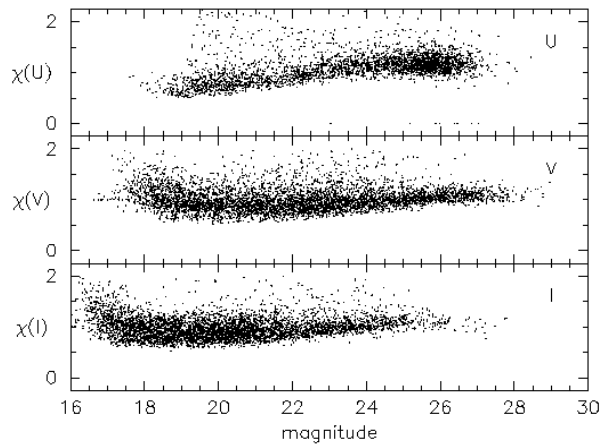


FIG. 6.— The panels show, from top to bottom, the dependence on magnitude for the U, V, and I photometry of the χ goodness of fit statistic for all stars in Table 5 that have magnitude error less than 1 and that were classified visually as stars.

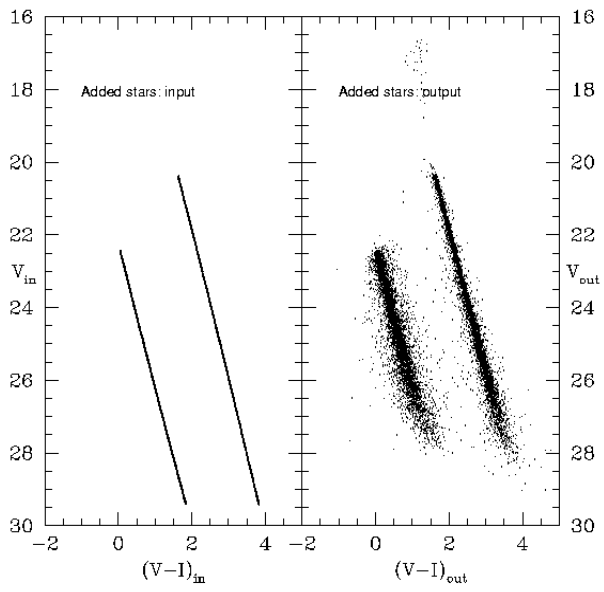


FIG. 7.— The left-hand panel shows the artificial star input sequences in V vs $V-I$. A total of $\sim 3 \times 10^4$ artificial stars were added. The right-hand panel shows the sum of the recovered sequences from all fields.